Differential heating: A versatile method for thermal conductivity measurements in high-energy-density matter

Y. Ping, A. Fernandez-Panella, H. Sio, A. Correa, R. Shepherd, O. Landen, R. A. London, P. A. Sterne, H. D. Whitley, D. Fratanduono, T. R. Boehly, and G. W. Collins

---

Articles you may be interested in

A simple differential steady-state method to measure the thermal conductivity of solid bulk materials with high accuracy
Rev. Sci. Instrum. **85**, 025108 (2014); 10.1063/1.4865111

Steady heat conduction-based thermal conductivity measurement of single walled carbon nanotubes thin film using a micropipette thermal sensor
Rev. Sci. Instrum. **84**, 034901 (2013); 10.1063/1.4792841

Technique for thermal conductivity measurements for organic materials over a wide temperature range
Rev. Sci. Instrum. **76**, 033908 (2005); 10.1063/1.1866252

Heat conduction nanocalorimeter for pl-scale single cell measurements
Appl. Phys. Lett. **80**, 2029 (2002); 10.1063/1.1457532

Data reduction in 3ω method for thin-film thermal conductivity determination
Rev. Sci. Instrum. **72**, 2139 (2001); 10.1063/1.1353189

Differential heating: A versatile method for thermal conductivity measurements in high-energy-density matter

Y. Ping,[1] A. Fernandez-Panella,[1] H. Sio,[2] A. Correa,[1] R. Shepherd,[1] O. Landen,[1] R. A. London,[1] P. A. Sterne,[1] H. D. Whitley,[1] D. Fratanduono,[1] T. R. Boehly,[3] and G. W. Collins[1]

[1]*Lawrence Livermore National Laboratory, Livermore, California 94550, USA*
[2]*Plasma Science and Fusion Center, Massachusetts Institute of Technology, Cambridge, Massachusetts 02139, USA*
[3]*Laboratory for Laser Energetics, University of Rochester, Rochester, New York 14623, USA*

We propose a method for thermal conductivity measurements of high energy density matter based on differential heating. A temperature gradient is created either by surface heating of one material or at an interface between two materials by different energy deposition. The subsequent heat conduction across the temperature gradient is observed by various time-resolved probing techniques. Conceptual designs of such measurements using laser heating, proton heating, and x-ray heating are presented. The sensitivity of the measurements to thermal conductivity is confirmed by simulations. © *2015 AIP Publishing LLC*. [http://dx.doi.org/10.1063/1.4929797]

I. INTRODUCTION

Thermal conductivity is one of the most fundamental and important physical properties of matter. It determines the heat transport rate and has an enormous impact on a variety of mechanical, electrical, chemical, and nuclear systems.[1] In high energy density (HED) matter that exists in planetary cores, astrophysical objects or fusion plasmas created in laboratories, the role of thermal conduction is exemplified in suppressing hydrodynamic instability growth in inertial confinement fusion (ICF) capsules,[2] affecting the overall implosion performance,[3] constraining the evolution of Earth's core-mantle boundary,[4] etc.

In ICF plasmas, suppressing hydrodynamic instability growth in capsules is of paramount importance to minimize the mix that is currently a major obstacle in achieving ignition.[5] The growth rate depends on many factors, including equations of state, opacity, diffusivity, viscosity, and thermal conductivity. Two-dimensional high-resolution hydrodynamical simulations using HYDRA[6] have shown that the hydro-instability growth is substantially decreased when using a higher thermal conductivity.[2] On the other hand, very high thermal conductivity of the ICF fuel would result in energy loss from the hot spot, thus deteriorating the overall performance of ICF implosion. The uncertainty in thermal conductivity has led to uncertainties in modeling and understanding ICF experiments. For example, recent calculations of DT thermal conductivity suggest a factor of 3–10 increase in comparison with previous models, and with the new values the total neutron yield varies up to 20%.[3]

Besides fusion plasmas, thermal conductivity also plays a role in planetary science. The conventional model of Earth's core evolution states that thermal convection in the core and the mantle has been the primary power source for geodynamo generation. However, recent calculations of iron thermal conductivity at Earth's core conditions are 2–3 times higher than the commonly used values.[7] In such a case, the

standard model of the core becomes questionable. It has been emphasized in a paper by Olson[4] that "High-pressure, high-temperature measurements are needed to pin down the actual conductivity of the core."

Despite the importance of thermal conductivity in HED systems, experimental measurements under relevant conditions are very scarce and challenging. In this paper, we propose a method of differential heating for thermal conductivity measurements and present conceptual designs for four different platforms. The paper is organized as follows: Sec. II describes the general concept of differential heating. Sec. III presents the detailed designs and corresponding diagnostics for heating by optical laser pulses, proton beams, line emission x-rays, and x-ray lasers, respectively. Finally, a summary is given in Sec. IV.

II. CONCEPT DESCRIPTION

The concept of differential heating is based on the definition of thermal conductivity: the heat flow rate in the presence of a temperature gradient. As illustrated in Fig. 1, a temperature gradient can be induced inside one material by surface heating (a), or between two materials by different energy deposition (b). In the former case, time-resolved measurements at the rear side will reveal the timing and amount of heat reaching the rear side which depends on the material's thermal conductivity. The surface heating technique has been used to measure thermal diffusivity in some low-energy-density systems.[8,9] For HED systems, the time scale is much faster, hence requiring diagnostics with much better time resolution, typically in the fs-ps range.

The 1D thermal conduction equation is

$$\rho C \frac{\partial T}{\partial t} = \frac{\partial}{\partial x} \kappa \frac{\partial T}{\partial x}, \tag{1}$$

where ρ is the mass density, C is the specific heat capacity per unit mass, and κ is the thermal conductivity. If ρ, C, and
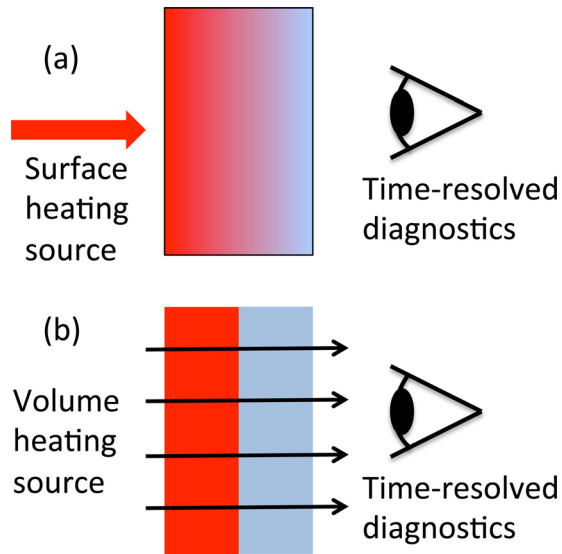
FIG. 1. Concept of differential heating in two schemes. (a) In one material, a temperature gradient is induced by surface heating. Time-resolved diagnostics will reveal the timing and amount of the heat flow reaching the rear side which depends on the material's thermal conductivity. (b) Between two materials, a temperature gradient is induced at the interface by different energy deposition in the two materials.

κ are all constants, for an ideal case with a boundary condition $T = T_s = const.$ at $x = 0$ and an initial condition $T = 0$ at $t = 0$ for all $x > 0$, this equation has an analytical solution,[10]

$$T(x,t) = T_s[1 - erf(x/\sqrt{4\alpha t})], \qquad (2)$$

where $\alpha = \kappa/(\rho C)$ is the thermal diffusivity, $erf(x)$ is the error function. Using x in unit of μm, t in ps, and α in $\mu m^2/ps$, Fig. 2(a) depicts the spatial profiles of the analytical solutions for $\alpha = 1$ at $t = 10 - 50$, showing the temperature gradient smearing out over time and the heat propagating away from x = 0. The time history of temperature at a distance $x_0 = 5$ is plotted in Fig. 2(b) for various α. Clearly, the time history strongly depends on α: for higher α, the temperature rise is earlier and faster at a fixed distance. Therefore, the thermal diffusivity or thermal conductivity can be measured by placing a witness plate at a certain distance or by observing the rear surface temperature of a finite-thickness target.

In reality ρ, C, and κ are not constants hence the conduction equation needs to be solved numerically. The high pressure in the HED material also leads to rapid expansion of the system. Therefore, $T(t)$ will result from the competition between thermal conduction heating and expansion cooling. From the analytical solution, it can be seen that the conduction time scales as x_0^2/κ, while a 1D expansion time scales linearly with x_0. Therefore, at shorter distances, thermal conduction can dominate over expansion at early times. For experimental design, the target thickness must be chosen carefully in order to measure the thermal conduction effect.

Based on Eq. (1), the specific heat also needs to be known in order to obtain thermal conductivity. At ambient conditions, the specific heat of a solid is approximately the Dulong-Petit limit, $3k_B$ per atom (k_B is the Boltzman constant). As temperature increases, the heat capacity usually increases as
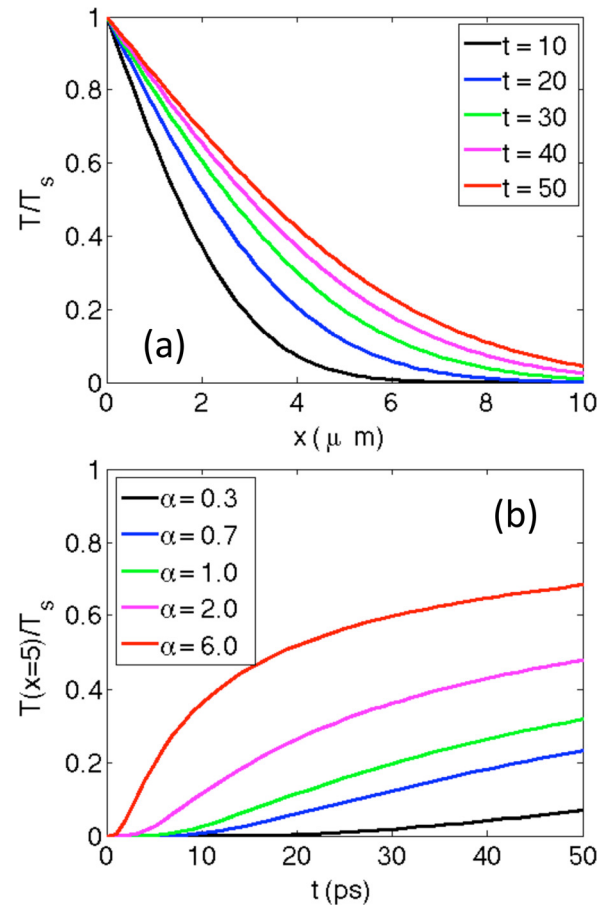

FIG. 2. (a) Analytical solutions of the thermal conduction equation at various delays. (b) The corresponding time history of temperature at $x = x_0 = 5$.

more electrons are ionized and contribute to the heat capacity. The constant-volume heat capacity of an ideal electron gas is $C_{V,e} = (3/2)n_e k_B$, where n_e is the electron density. From an experimental point of view, if the plasma is fully ionized, weakly coupled, and classical, these experiments can be performed in a regime where the specific heat is known. On the other hand, at lower temperatures and under conditions of partial ionization, these measurements will provide data to benchmark models of the specific heat and thermal conductivity that are computed self-consistently.

In the case of two materials, differential heating can be achieved either by x-rays for materials with different opacities or by particles for materials with different stopping powers. Similar to the one-material case, the thermal conduction can be observed either at the rear side of the cooler material or more directly at the interface with high-resolution radiography. In Sec. III, conceptual designs are presented for four platforms using various time-resolved diagnostics.

III. VARIOUS PLATFORMS

A. Laser heating

For heating with optical lasers at intensities $10^{12} - 10^{13}$ W/cm^2, the heated region is mainly limited by the optical penetration depth and the ballistic distance of excited electrons,[11–13] which is typically on the order of tens of nanometers in solid metal foils[14] for subpicosecond laser
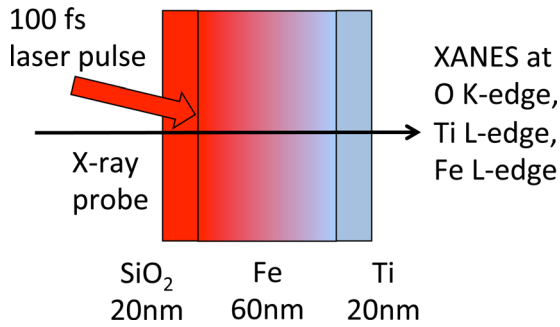
FIG. 3. A target design for thermal conductivity measurements by optical laser heating and XANES probe.

duration. A target design for measuring thermal conductivity of laser-heated Fe is shown in Fig. 3. The target consists of three layers: 20 nm SiO$_2$, 60 nm Fe, and 20 nm Ti. The SiO$_2$ and Ti serve as tamping layers to maintain the solid density of Fe as well as witness layers to monitor temperature at the front and rear sides of the Fe. Their thickness is thin enough to ensure minimal gradient inside the witness layers. The optical laser is incident from the SiO$_2$ side onto the Fe surface due to the transparency of SiO$_2$. The thickness of Fe (60 nm) is larger than the ballistic heating distance in Fe ($\sim$20 nm) so that a temperature gradient is induced inside the Fe layer. It is strongly desired to use an optical laser pulse with a duration as short as possible, on the order of 100 fs, to minimize hydrodynamic expansion during heating.

The probing technique is x-ray absorption near edge structure (XANES) which offers material selectivity so that the temperature at the front and rear sides of the Fe can be measured as a function of time. XANES has been developed as a temperature diagnostic by observing the temperature-induced smearing of an absorption edge.[15,16] The measurements can be performed at synchrotron facilities, such as Advanced Light Source (ALS) at Lawrence Berkeley National Laboratory, using a fast streak camera for the O K-edge at 543 eV (Ref. 17) and the Ti L_3-edge at 454 eV.[16] The Fe L_3-edge at 707 eV can also be measured for a spatially averaged temperature in Fe to provide further constraints. These edges are far away enough from each other so that measurements at each edge can be performed without interference. There are a few beamlines at ALS equipped with fs laser systems, such as 6.0.2 and 11.0.1, that are suitable for the ultrafast heating.

A widely used model for such an ultrafast laser-solid interaction is the two-temperature model (TTM),

$$C_e \frac{\partial T_e}{\partial t} = \frac{\partial}{\partial x} \kappa_e \frac{\partial T_e}{\partial x} - G(T_e - T_i) + S_L(x,t), \quad (3)$$

$$C_i \frac{\partial T_i}{\partial t} = \frac{\partial}{\partial x} \kappa_i \frac{\partial T_i}{\partial x} + G(T_e - T_i), \quad (4)$$

where C_e and C_i are heat capacities per unit volume of electrons and ions, respectively. G is the electron-ion coupling rate and $S_L(t)$ is the source term for laser heating. Upon interaction with subpicosecond laser pulses, the electrons are heated first and the ions stay cold initially, establishing a non-equilibrium system. The electrons subsequently transfer

their energy to ions through e-ion coupling (the G term). This setup has been employed to measure e-ion equilibration time.[16] For simulations using the TTM, we adopt the temperature-dependent $C_e(T_e)$ and $G(T_e)$ from Ref. 18, which agree well with previous experimental data.[16]

The two equations are numerically solved to study the sensitivity of the observables to thermal conductivity of Fe. For simplicity, the front SiO$_2$ layer is not included since the laser energy is deposited mostly into the Fe layer, and the density is kept at the solid density, which is maintained by the tamping layers. The temperature of the back Ti layer only reaches a few thousand K, hence the expansion is negligible in the first 10 ps. The thermal conduction term in the ion equation is also ignored because κ_i is more than an order of magnitude less than κ_e. The Dulong-Petit limit is used for C_i. Fig. 4(a) shows spatial profiles of the temperature in Fe (0–60 nm) and Ti (60–80 nm) at four delays for an incident laser intensity of $I_0 = 1 \times 10^{13}$ W/cm^2 and a pulse duration 100 fs at FWHM. x = 0 is the Fe front surface irradiated by the laser. The laser energy deposition is modeled as $S_L(x,t) = I_0 \exp(-x/L_b)$, where L_b is the ballistic distance. At t = 0.5 ps, the heating is completed with a maximum temperature 8 eV at the front and a penetration depth similar to the ballistic distance 20 nm. The temperature spatial profile is similar but not the same as the laser deposition profile because of temperature-dependent electron heat capacity. The front layer measurements can constrain the ballistic distance since the maximum front temperature is inversely proportional to L_b in Fe. After heating, the temperature profile relaxes over time due to conduction and e-ion coupling. The heat flow reaches the Ti layer after 3 ps if using Sesame table 22144 for the Fe thermal conductivity. It should be noted that the e-ion coupling in Fe can be measured independently using a similar target but with 20 nm Fe so that the temperature is uniform inside Fe, similar to the method in previous experiments on Cu.[16]

Fig. 4(b) shows the predicted thermal conductivities of Fe at solid density by three models, Lee-More,[19] Sesame table 22144,[20] and Purgatorio.[21] The predictions vary as much as 8 times in this few eV regime. These three thermal conductivities are plugged into the TTM calculations to show the effect of Fe thermal conductivity on the temperature of the back Ti layer. Fig. 4(c) shows the time history of the space-averaged Ti temperature. The onset of the temperature rise is at 2 ps for Purgatorio, 4 ps for Sesame 22144, and much longer than 10 ps for Lee-More. This time difference can be resolved by ultrafast x-ray streak cameras.[22] To confirm that this onset depends mainly on Fe thermal conductivity and not on the properties of Ti, we varied the C_e, κ_e, and G of Ti and the results are plotted in Fig. 4(c) as dashed and dotted-dashed lines. It is clear that the onset time does not change with Ti properties, but is most sensitive to $\kappa_{e,Fe}$ since this is when the heat flow from Fe reaches Ti. Therefore, the validity of thermal conductivity models can be tested by measuring the Ti temperature vs time by streaked XANES.

B. Proton heating

Volumetric heating of bulk materials can be achieved by high energy particles, such as a proton beam generated by
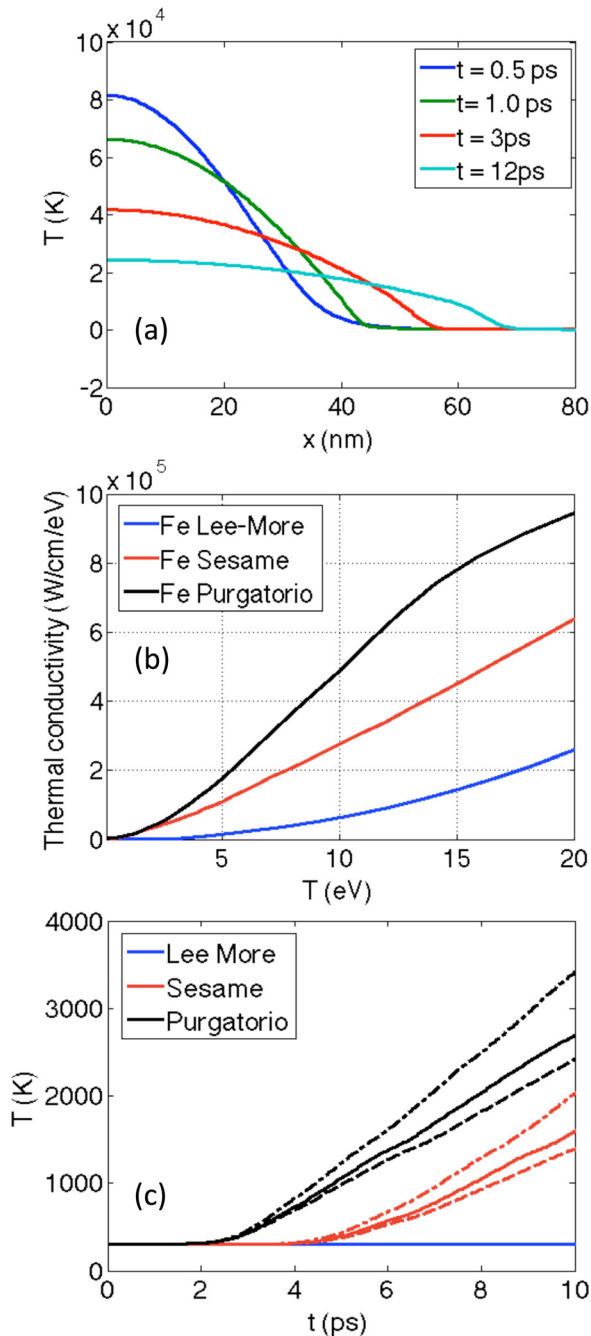
FIG. 4. (a) Spatial profiles of the electron temperature at four delays from TTM calculations with Sesame conductivity. (b) Thermal conductivity of iron at solid density predicted by three models, Lee-More,[19] Sesame table 22 144,[20] and Purgatorio.[21] (c) The spatially averaged temperature of Ti layer vs time. The dashed and dotted-dashed lines are from simulations with κ_{Ti} varied by $0.3\times$ and $3\times$, respectively. Varying other properties of Ti, such as C_e and G, results in less difference than those shown.

short-pulse interaction with foils.[23,24] The energy deposition of protons strongly depends on the properties of the material, in particular, the electron density and ionization potential. Therefore, proton heating of an interface between two materials with very different properties can result in a sharp temperature gradient between the two materials. The Bethe formula of the energy loss for a particle with velocity v and charge z in a material with electron density n_e and ionization potential E_{ion} is[25]
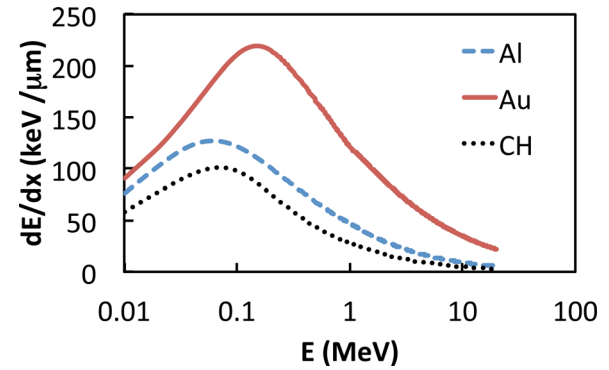

FIG. 5. Stopping power of protons in Au, Al and CH. The energy range of 0.1–1 MeV is most effective for proton differential heating.

$$\frac{dE}{dx} = -\frac{4\pi n_e z^2}{m_e v^2}\left(\frac{e^2}{4\pi\epsilon_0}\right)^2\left[ln\left(\frac{2m_e v^2}{E_{ion}(1-v^2/c^2)}\right)-\frac{v^2}{c^2}\right]. \quad (5)$$

At ambient conditions, this formula works well at high particle energies and needs corrections for partial ionization and screening effects at low energies.[26] The general trend is that the material with a higher Z has a stronger stopping power than low-Z materials. Fig. 5 shows the stopping power of protons in Au, CH, and Al calculated using SRIM (Stopping and Range of Ions in Matter).[27] It is clear that protons will deposit more energy in Au than in CH, and the energy range of 0.1–1 MeV is most effective for differential proton heating.

An experimental design using proton heating is illustrated in Fig. 6. The target is made of a free-standing Cu foil for proton generation by target normal sheath acceleration (TNSA),[28] and a bi-layer Au/CH foil supported by a 100 nm Si_3N_4 window. The thickness of the Au and CH layers should be small enough so that the thermal conduction is dominant over expansion cooling, as described in Sec. II. Hydrodynamic simulations using HYADES[29] indicate that a proper thickness is in the range of 40–200 nm. The heat flow will be detected at the rear surface of the CH layer by streaked optical pyrometry (SOP). At the same time, the CH surface expansion and reflectivity can be measured by chirped pulse Fourier domain interferometry (FDI).[13,30]

The HYADES simulation results on the heating are presented in Fig. 7. A measured proton energy spectrum from a previous Titan experiment,[24] plotted in Fig. 7(a), is used as the heating source in HYADES simulations with stopping
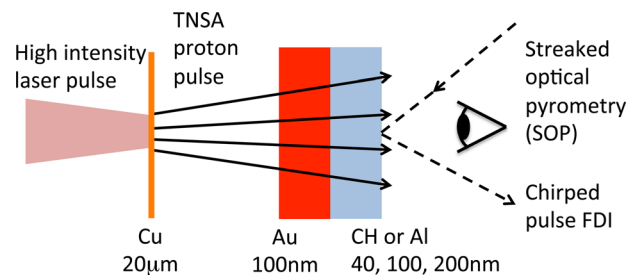

FIG. 6. Experimental schematic for proton heating. The protons are generated by TNSA through laser irradiating a Cu foil at high intensities. After traveling a vacuum gap, the protons deposit some energy into the second target with the dual-layer for differential heating.

powers from SRIM. The duration of the proton pulse is determined by the time-of-flight across the distance between the TNSA foil and the Au/CH foil, which is chosen to be $50\,\mu m$, much shorter than previous experiments in order to minimize the heating time. If the heating is long and slow, the thermal conduction occurs at the same time as the hydrodynamic expansion which will smear out the observations. Fig. 7(b) shows the proton energy deposition as a function of
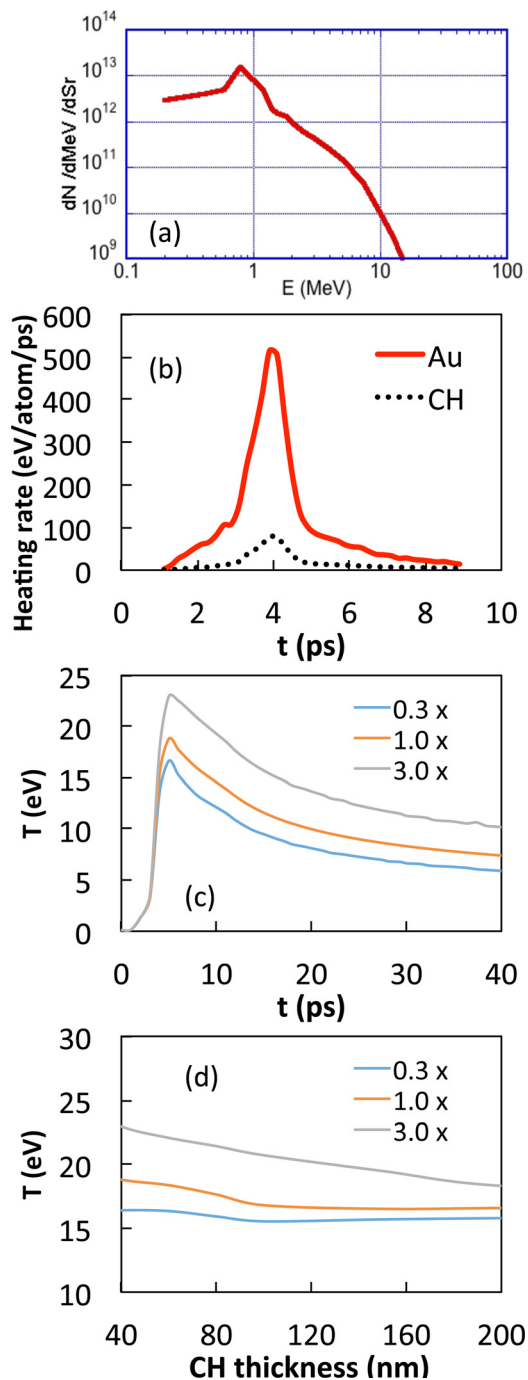

FIG. 7. (a) A proton energy spectrum measured in a Titan experiment,[24] which is used as the heating source in simulations. (b) Simulated energy deposition in the target of 100 nm Au plus 40 nm CH on a 100 nm Si_3N_4 window. The stopping power is from SRIM.[27] (c) Simulated time history of the CH surface temperature with three multipliers in κ, 0.3, 1.0, and 3.0. (d) The maximum CH surface temperature vs CH thickness for the three multipliers.

time in Au and CH, respectively. The heating lasts about 6 ps, with higher energy deposition in Au as expected. Fig. 7(c) displays the time history of the CH surface temperature for 40 nm CH thickness using various CH thermal conductivities. Because κ is not a constant but a function of both density and temperature, it is varied by applying a multiplier in all regions to test the sensitivity. The three curves in Fig. 7(c) are for multipliers 0.3, 1.0, and 3.0. As κ changes by a factor of 3, the maximum temperature of the CH surface varies by $\sim$3–5 eV, which is detectable by SOP with error bars ± 2 eV from the previous Titan experiment.[24] The error bars can be further reduced by repeating shots. The CH thickness can also be varied to verify the decay of the heat flow, as shown in Fig. 7(d). For the three multipliers in κ, the decay vs thickness is quite different, providing further constraint on the thermal conductivity.

To confirm that thermal conduction is the dominant transport process over radiation for this design, we also performed simulations with radiation on or off. The difference is negligible. For SOP measurements, the opacity of the CH layer should be taken into account. Based on the HYADES simulation, CH is ionized to $n_e = 6 \times 10^{22}\,cm^{-3}$ within the first 3 ps. The skin depth at this electron density is $c/\omega_{pe} \sim 20$ nm, which sets the lower limit of the CH thickness. The experiment can therefore be carried out for 40 nm, 100 nm, and 200 nm CH layers.

It should be noted that the stopping power would change when materials are heated up so that more accurate simulations would require self-consistent stopping power calculations, which is beyond the scope of this paper. Other concerns include space charge effects due to hot electrons generated by the intense laser-plasma interaction, which could contribute to heating. Nonetheless, these issues will alter the resulting temperature gradients but will not eliminate the thermal conduction. Such an experiment can be readily carried out in medium-scale laser facilities, such as Titan at LLNL and Trident laser at LANL to test this idea for thermal conductivity measurements in warm dense matter (WDM).

C. Laser-generated x-ray heating

Alternative to proton heating, volumetric heating can also be achieved by x-rays. Laser-generated x-rays have been proven to be a good source as well as a good probe. The typical conversion efficiency from ns laser pulses into $H_{e\alpha}$ lines is $0.1\% - 5\%$ at 2–7 keV.[31] The conversion efficiency is usually higher for L-band, reaching a few percent[32] with a large bandwidth, which is suitable for heating. In general, large laser facilities are required to reach temperatures well above 1 eV. A design for differential heating of CH and Be by laser generated x-rays has been published in a previous paper.[33] Here, we present a design for CH and D_2 which has direct relevance to ICF targets.

Besides experimental challenges in dealing with cryogenic cells, x-ray heating of D_2 is difficult because D_2 is transparent to most x-rays unless highly compressed. To measure thermal conductivity of D_2 at WDM conditions, we employ a scheme of heating the CH first with soft x-rays, followed by shock heating and compression of D_2 driven by the
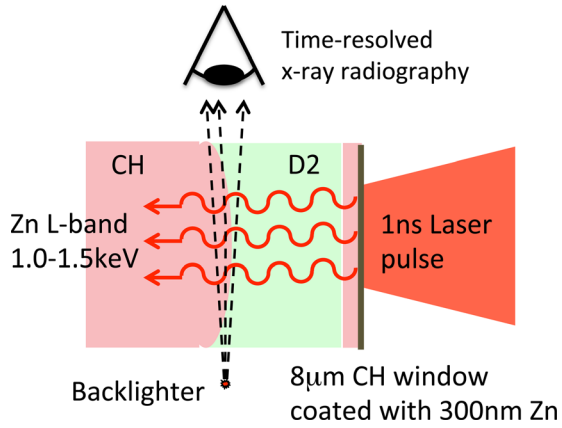
FIG. 8. Schematic of the target and the experimental setup for thermal conductivity measurements of D_2 by laser-generated x-ray heating. The backlighter x-rays are bent at the CH/D_2 interface due to refraction by the density gradient.

FIG. 9. Contour plots of temperature (a) and density (b) vs time and space for the CH/D_2 design. The interface is marked as the red dashed line. The heated CH drives a shock into D_2 which compresses and heats D_2.

heated CH. The target design is illustrated in Fig. 8. The x-rays are generated by laser irradiating a Zn foil coated on the $8\,\mu m$ CH window of the cryogenic cell containing D_2. The Zn L-band emission as well soft x-rays from laser-plasma interaction region will go through $800\,\mu m$ D_2 to preferentially heat a CH cylinder at the back of the cell. The evolution of the curved CH/D_2 interface will be probed by refraction enhanced x-ray radiography[33] using 2.8 keV Cl $H_{e\alpha}$ line. At x-ray energies well above any absorption edges, the refractive index is only a function of the total electron density.[34] Therefore, ionization does not affect the radiographic measurements here. The CH surface is cylindrically curved to $R = 1\,mm$ to eliminate alignment uncertainty and to enhance the contrast.[35] The radius of curvature is much larger than the typical scale lengths near the CH/D_2 interface so that the hydrodynamics near the interface can still be approximated as a 1D system.

The evolution of the target temperature and density is shown in the contour plots in Fig. 9. For this 1D simulation using HYADES, the laser intensity is $5 \times 10^{14}\,W/cm^2$, with injected 1.1 keV x-rays at $1 \times 10^{13}\,W/cm^2$ (2% conversion efficiency). Both laser and the x-rays are incident from the right hand side. At the end of the x-ray heating (1 ns), CH near the interface reaches ~50 eV and D_2 temperature stays low. The heated CH drives a shock into D2, which heats D_2 to ~5 eV and compresses to 0.5 g/cc. As time evolves, the temperature and density gradients at the interface become longer due to thermal conduction. After 4 ns, the shock driven by the laser ablation of the CH window at the other side approaches the curved interface region, which will interfere with the interface. Hence, the best timing for the radiography measurements is at 4 ns. The thickness of D_2 ($800\,\mu m$) is chosen to delay the laser-driven shock so that the thermal conduction effect on the interface gradient is fully developed and detectable before the arrival of this shock.

The temperature and density profiles near the interface at 4 ns are plotted in Figs. 10(a) and 10(b) for three thermal conductivity multipliers in D_2, 0.3, 1.0, and 3.0. The interface is at x = 0. The temperature is 40 eV at the CH side and 5 eV at the D_2 side. The density of CH is released to below
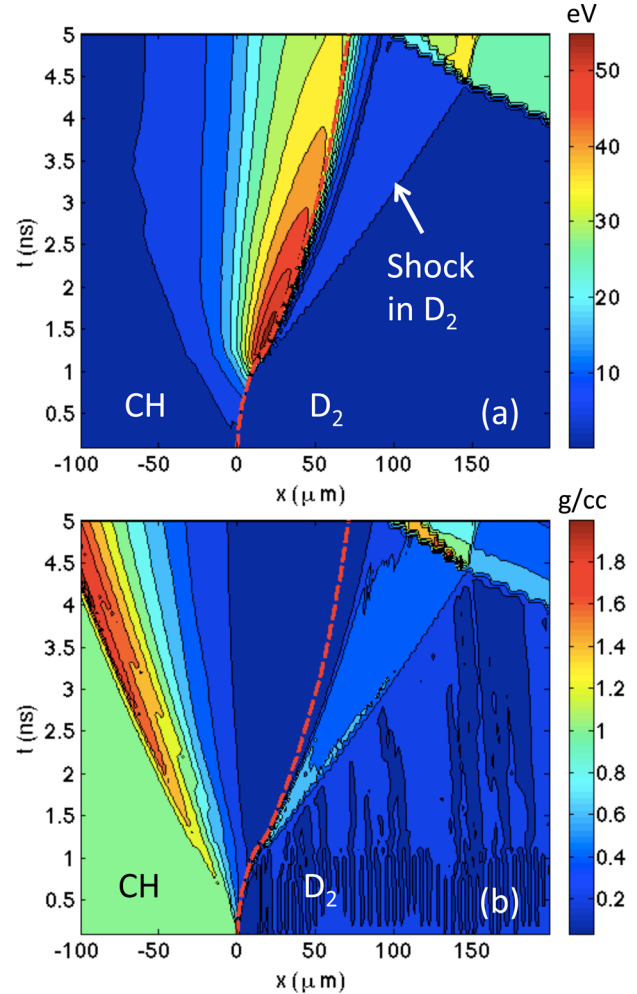
0.1 g/cc, and the D_2 density is compressed to close to 0.5 g/cc. The gradient near the interface clearly depends on the thermal conductivity, the higher κ, and the longer the gradient. The simulated radiograph lineouts using ray-tracing at 2.8 keV are displayed in Fig. 10(c). The difference is observable by the refraction enhanced radiograph technique because of its high spatial sensitivity.[33] To examine the radiation effect at the interface, we also carried out simulations with conduction off or radiation off after the heating. The comparison is shown in Fig. 10(d). Compared to the normal case of both conduction and radiation on (blue dashed line), turning off conduction results in a much sharper gradient at the interface with a small pedestal (red line). If the radiation is turned off after the heating, the gradient is similar to the normal case but the pedestal disappears (green line), indicating that the small pedestal is generated by radiation transport. These results confirm that the gradient is dominated by thermal conduction process therefore the radiographic measurements are sensitive to D_2 thermal conductivity. In addition to measuring the density profiles by the radiography, the shock velocity and the interface velocity can also be measured to constrain the temperature in D_2 and CH. Measurements at various delays should be performed to

follow the evolution of the interface, which is important to minimize reliance on equation-of-state models.

This experiment is suitable for OMEGA or OMEGA EP facilities at LLE. To minimize the motion blurring at the
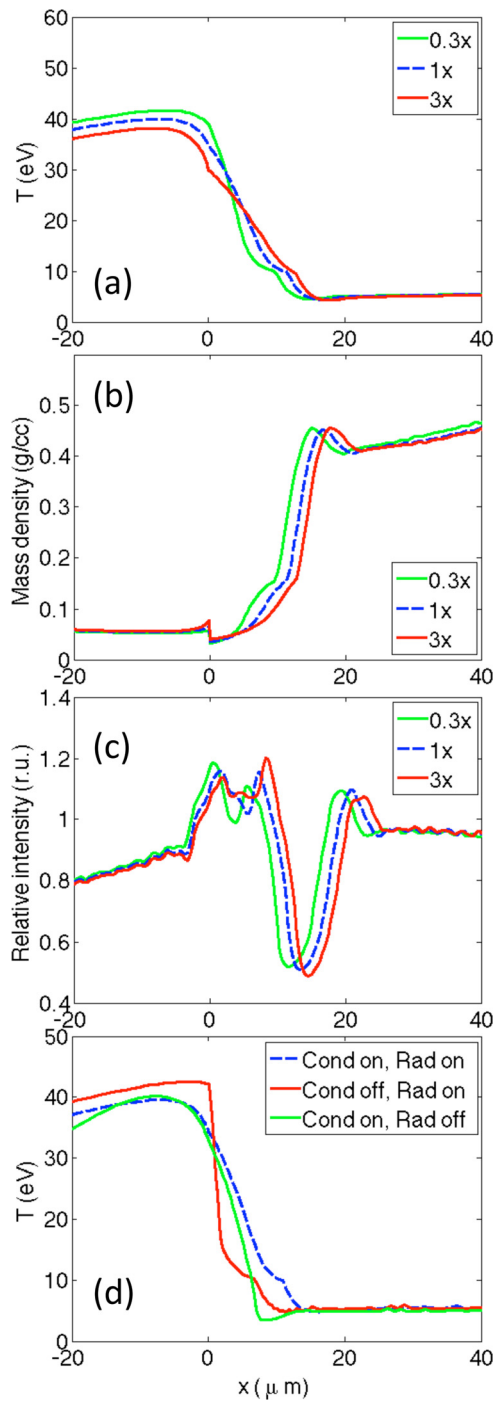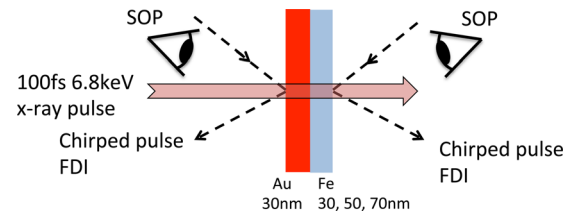

FIG. 11. Experimental schematic for a Au/Fe target on a XFEL platform.

interface in the radiographs, a backlighter created by the OMEGA EP short pulse would be a better choice. The interface moves at $\sim 10\,\mu m/ns$ so that the image can also be frozen with a 100 ps gated or streak camera. A planar cryogenic cell has been designed and tested at LLE (Laboratory for Laser Energetics), which can be used for these measurements.

D. XFEL heating

The advancement in X-ray Free Electron Laser (XFEL) facilities opens new routes to create and probe HED matter. For differential heating, this platform provides a unique combination of prompt (~ 100 fs) and volumetric heating of mid- to high-Z materials. The x-ray photon energy is tunable to
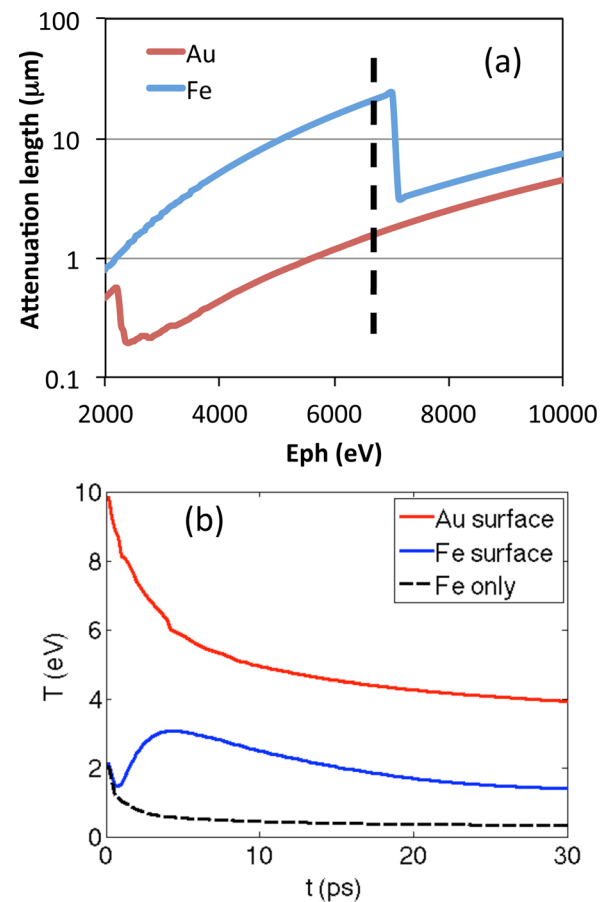

FIG. 12. (a) X-ray attenuation lengths in Au and Fe. The dashed line marks the chosen x-ray energy just before Fe K-edge for differential heating. (b) Time history of the temperature at front Au side of an Au/Fe target (red), at the rear Fe side (blue), and at the rear side of an Fe only target (black dashed line). The temperature rise in Fe (red line) is caused by heat flow from the hotter Au layer, which is absent in case of a Fe only target.

FIG. 10. Temperature (a) and density (b) profiles near the CH/D_2 interface at 4 ns using three thermal conductivities. The interface is set at x = 0. (c) Simulated radiograph lineouts by ray tracing at 2.8 keV for the three density profiles in (b). The difference is measurable. The ray-tracing used a source-object distance of 10 mm, an object-detector distance of 600 mm, and source size 5 μm. For better comparison with other profiles, the lineout is scaled back to the object plane by the magnification of 60$\times$. (d) Effect of radiation by comparing three cases: both radiation and conduction are on (blue dashed line), conduction off and radiation on (red solid line), and conduction on and radiation off (green solid line). The temperature gradient at the interface is dominated by thermal conduction, while the radiation transport leads to a small pedestal at the D_2 side.

selectively heat a particular material. The prompt heating maximizes the temperature gradient as well as minimizing hydrodynamic motion during the heating, hence providing an ideal case for thermal conductivity measurements.

Fig. 11 shows a setup for a Au/Fe target. It is a simple approach using an x-ray pump plus an optical probe. Similar to the proton heating experiment, the diagnostics are SOP and FDI which measure the surface brightness temperature, the reflectivity/emissivity, and the expansion velocity. The open geometry of XFEL heating allows simultaneous measurements on both front and rear surfaces. We propose heating with x-rays at 6.8 keV, just below the Fe K-edge, where the absorption lengths in Au and Fe differ by an order of magnitude as shown in Fig. 12(a). The thickness of Au and Fe are both 30 nm, much less than the attenuation lengths in the two materials. Therefore, heating is uniform in each material while a temperature gradient is created between the two materials.

The time history of the temperature at Au and Fe surfaces from HYADES simulations is plotted in Fig. 12(b). The x-ray pulses are 1 mJ, 100 fs, and focused to $\sim$10 μm at an on-target intensity of $\sim$$10^{16}$ W/cm^2. Initially Au and Fe are heated to 10 eV and 2 eV, respectively. At the Au surface, the temperature decreases monotonically over time due to expansion cooling (red solid line). At the Fe surface, on the other hand, the temperature decreases for about 1 ps and

then increases due to the heat flow from the hotter Au (blue solid line). For a comparison, a simulation with Fe only target without the Au layer is also performed and the time history is plotted as the black dashed line in Fig. 12(b), showing a similar initial temperature 2 eV in Fe by the x-ray heating and monotonic decrease over time. This confirms that the temporal rise in Fe surface temperature is induced by thermal conduction.

To compare the three conductivity models shown in Fig. 4(b), the time history of the Fe surface temperature is plotted in Fig. 13(a). The higher thermal conductivity in Purgatorio model leads to higher and earlier temperature increase in time. The different predictions by the three models are clearly distinguishable by the optical pyrometry measurements using ultrafast optical streak cameras with $\leq$ 2 ps time resolution which are commercially available. To provide further constraints on the thermal conductivity, the thickness of the Fe layer can also be varied. As the heat conducts through a thicker layer, the heat flow decays and the temporal rise is delayed, as shown in Fig. 13(b). This series of measurements vs thickness would provide a consistency check on a relative basis. Furthermore, the reflectivity data from FDI can be used to obtain electrical conductivity σ. Measurements of both thermal and electrical conductivities would offer an opportunity to test the Wiedemann-Franz law, $\kappa/\sigma \propto T$, in WDM.

IV. CONCLUSION

We have described the concept of differential heating for thermal conductivity measurements in the WDM regime, and presented experimental designs for four platforms using optical laser heating, proton heating, laser-generated x-ray heating, and XFEL heating. Each platform has its own pros and cons. The optical laser heating with XANES probe is suitable for metals for which the TTM model is valid. The temperature sensitivity of XANES allows for detecting <1000 K change. The applicable temperature range is from a few thousand K to a couple of eV. At above 10 eV, the system expansion is substantial and the density effect in XANES spectra has to be taken into account. The proton heating requires two materials with different stopping powers. We have found that Au and a low-Z material such as Al or CH provide a good pair for these measurements. The temperature range is on the order of 1 eV to tens of eV where SOP has enough sensitivity to temperature. Self-consistent stopping power calculations in heated materials are needed for accurate modeling. Some space charge effects induced by hot electrons accompanying the TNSA proton beam may need to be minimized in order to measure thermal conductivity. The laser-generated x-ray heating has been demonstrated for a CH/Be interface on OMEGA laser. This is the only platform where the evolution of the interface is directly observed by high resolution x-ray radiography. Measurements of D_2 thermal conductivity are directly relevant to ICF experiments yet most challenging due to cryogenic requirements and difficulties in heating D_2. A design for CH/D_2 is described to show distinguishable radiographs when the thermal conductivity of D_2 is varied by a factor of 3. Finally, the XFEL platform offers ultrafast bulk
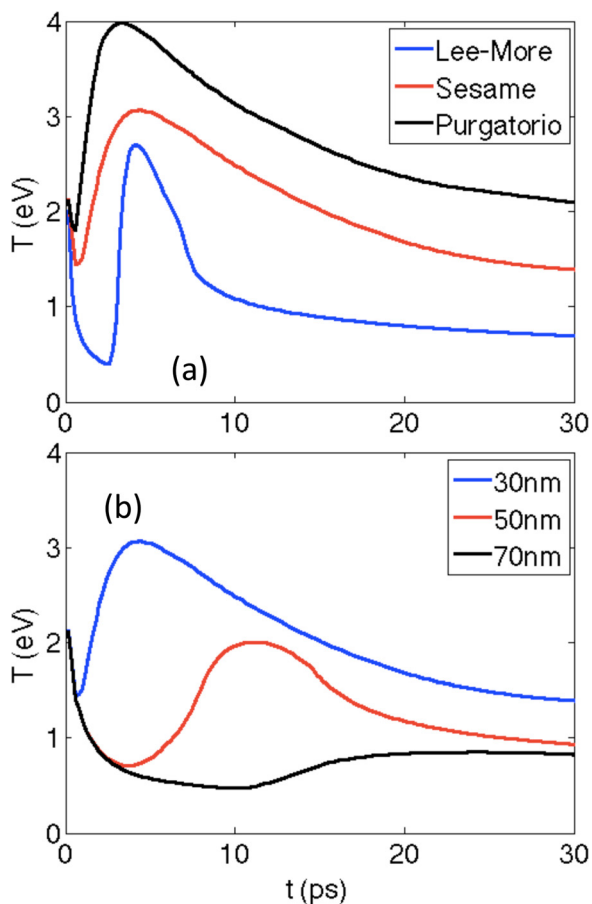

FIG. 13. (a) Simulated time history of the Fe surface temperature using three models. (b) The surface temperature of the Fe layer with varying thickness, 30, 50, and 70 nm.

heating which is ideal to minimize hydrodynamic motion during heating. The material pairs are determined by the x-ray energy range. Differential heating of a Au/Fe target can provide benchmarking data to validate three commonly used models, Lee-More, Sesame and Purgatorio. We expect that the concept of differential heating will enable thermal conductivity study of WDM and the designs will promote experiments on these challenging measurements.

ACKNOWLEDGMENTS

[1]T. M. Tritt, *Thermal Conductivity: Theory, Properties and Applications* (Springer, 2004).

[2]B. A. Hammel, S. W. Haan, D. S. Clark, M. J. Edwards, S. H. Langer, M. M. Marinak, M. V. Patel, J. D. Salmonson, and H. A. Scott, High Energy Density Phys. **6**, 171 (2010).

[3]S. X. Hu, L. A. Collins, T. R. Boehly, J. D. Kress, V. N. Goncharov, and S. Skupsky, Phys. Rev. E **89**, 043105 (2014).

[4]P. Olson, Science **342**, 431 (2013).

[5]O. Hurricane, D. A. Callahan, D. T. Casey, P. M. Celliers, C. Cerjan, E. L. Dewald, T. R. Dittrich, T. Doppner, D. E. Hinkel, L. F. Berzak Hopkins, J. L. Kline, S. Le Pape, T. Ma, A. G. MacPhee, J. L. Milovich, A. Pak, H.-S. Park, P. K. Patel, B. A. Remington, J. D. Salmonson, P. T. Springer, and R. Tommasini, Nature **506**, 343 (2014).

[6]M. M. Marinak, G. D. Kerbel, N. A. Gentile, O. Jones, D. Munro, S. Pollaine, T. R. Dittrich, and S. W. Haan, Phys. Plasmas **5**, 1125 (1998).

[7]M. Pozzo, C. Davies, D. Gubbins, and D. Alfe, Nature **485**, 355 (2012).

[8]P. Beck, A. F. Goncharov, V. V. Struzhkin, B. Militzer, H. K. Mao, and R. J. Hemley, Appl. Phys. Lett. **91**, 181914 (2007).

[9]B. M. La Lone, G. Capelle, G. D. Stevens, W. D. Turley, and L. R. Veeser, Rev. Sci. Instrum. **85**, 073903 (2014).

[10]H. S. Carslaw and J. C. Jaeger, *Conduction of Heat in Solids* (Oxford, 1986).

[11]T. Ao, Y. Ping, K. Widmann, D. F. Price, E. Lee, H. Tam, P. T. Springer, and A. Ng, Phys. Rev. Lett. **96**, 055001 (2006).

[12]Y. Ping, D. Hanson, I. Koslow, T. Ogitsu, D. Prendergast, E. Schwegler, G. Collins, and A. Ng, Phys. Rev. Lett. **96**, 255003 (2006).

[13]T. Ogitsu, Y. Ping, A. Correa, B. Cho, P. Heimann, E. Schwegler, J. Cao, and G. W. Collins, High Energy Density Phys. **8**, 303–306 (2012).

[14]J. Hohlfeld, S. S. Wellershoff, J. Gdde, U. Conrad, V. Janke, and E. Matthias, Chem. Phys. **251**, 237 (2000).

[15]A. Mancic, A. Levy, M. Harmand, M. Nakatsutsumi, P. Antici, P. Audebert, P. Combis, S. Fourmaux, S. Mazevet, O. Peyrusse, V. Recoules, P. Renaudin, J. Robiche, F. Dorchies, and J. Fuchs, Phys. Rev. Lett. **104**, 35002 (2010).

[16]B. I. Cho, K. Engelhorn, A. A. Correa, T. Ogitsu, C. P. Weber, H. J. Lee, J. Feng, P. A. Ni, Y. Ping, A. J. Nelson, D. Prendergast, R. W. Lee, R. W. Falcone, and P. A. Heimann, Phys. Rev. Lett. **106**, 167601 (2011).

[17]K. Engelhorn, V. Recoules, B. I. Cho, B. Barbrel, S. Mazevet, D. M. Krol, R. W. Falcone, and P. A. Heimann, Phys. Rev. B **91**, 214305 (2015).

[18]Z. Lin, L. V. Zhigilei, and V. Celli, Phys. Rev. B **77**, 075133 (2008).

[19]Y. T. Lee and R. M. More, Phys. Fluids **27**, 1273 (1984).

[20]K. S. Holian, Los Alamos National Laboratory, Los Alamos, New Mexico, Report No. LA-10160-MS UC-34, 1984.

[21]B. Wilson, V. Sonnad, P. Sterne, and W. Isaacs, J. Quant. Spectrosc. Radiat. Transfer **99**, 658 (2006).

[22]J. Feng, K. Engelhorn, B. I. Cho, H. J. Lee, M. Greaves, C. P. Weber, R. W. Falcone, H. A. Padmore, and P. A. Heimann, Appl. Phys. Lett. **96**, 134102 (2010).

[23]P. K. Patel, A. J. Mackinnon, M. H. Key, T. E. Cowan, M. E. Foord, M. Allen, D. F. Price, H. Ruhl, P. T. Springer, and R. Stephens, Phys. Rev. Lett. **91**, 125004 (2003).

[24]G. M. Dyer, A. C. Bernstein, B. I. Cho, J. Osterholz, W. Grigsby, A. Dalton, R. Shepherd, Y. Ping, H. Chen, K. Widmann, and T. Ditmire, Phys. Rev. Lett. **101**, 015002 (2008).

[25]H. A. Bethe and W. Heitler, Proc. R. Soc. London, Ser. A **146**, 83 (1934).

[26]F. Bloch, Z. Phys. **81**, 363 (1933).

[27]J. F. Ziegler, J, P. Biersack, and U. Littmark, "The stopping and range of ions in solids," Vol. 1 of series, *Stopping and Ranges of Ions in Matter* (Pergamon Press, New York, 1984).

[28]S. C. Wilks, A. B. Langdon, T. E. Cowan, M. Roth, M. Singh, S. Hatchett, M. H. Key, D. Pennington, A. MacKinnon, and R. A. Snavely, Phys. Plasmas **8**, 542 (2001).

[29]J. T. Larsen and S. M. Lane, J. Quant. Spectrosc. Radiat. Transfer **51**, 179 (1994).

[30]S. Rebibo, J. P. Geindre, P. Audebert, G. Grillon, J. P. Chambaret, and J. C. Gauthier, Laser Part. Beams **19**, 67 (2001).

[31]D. Babonneau, M. Primout, F. Girard, J. P. Jadaud, M. Naudy, B. Villette, S. Depierreux, C. Blancard, G. Faussurier, K. B. Fournier, L. Suter, R. Kauffman, S. Glenzer, M. C. Miller, J. Grun, and J. Davis, Phys. Plasmas **15**, 092702 (2008).

[32]N. Izumi, E. Dewald, B. Kozioziemski, O. L. Landen, and J. A. Koch, Fusion Sci. Technol. **55**, 253 (2009).

[33]Y. Ping, O. L. Landen, D. G. Hicks, J. A. Koch, R. Wallace, C. Sorce, B. A. Hammel, and G. W. Collins, J. Instrum. **6**, P09004 (2011).

[34]B. L. Henke, E. M. Gullikson, and J. C. Davis, "X-ray interactions: Photoabsorption, scattering, transmission, and reflection at E = 50–30 000 eV, Z = 1–92," At. Data Nucl. Data Tables **54**, 181 (1993).

[35]J. A. Koch, O. L. Landen, B. J. Kozioziemski, N. Izumi, E. L. Dewald, J. D. Salmonson, and B. A. Hammel, J. Appl. Phys. **105**, 113112 (2009).